https://dx.doi.org/10.21577/0103-5053.20220144

J. Braz. Chem. Soc., Vol. 34, No. 5, 734-744, 2023

Article

Nickel Nanoparticles Anchored on Bentonite Clay for Methane Decomposition with Ordered Carbon as a Product

Rayssa J. B. Motta, *[a,b] *Camila B. Dornelas*[b] *and Rusiene M. de Almeida*[a]

[a]*Grupo de Catálise e Reatividade Química (GCAR), Instituto de Química e Biotecnologia, Universidade Federal de Alagoas, 57072-970 Maceió-AL, Brazil*

[b]*Laboratório de Tecnologia de Nanossistemas Carreadores de Substâncias Ativas (TECNANO), Departamento de Farmácia, Universidade Federal de Alagoas, 57072-970 Maceió-AL, Brazil*

Catalysts were synthesized with Ni and bentonite clay, without previous treatment, through wet impregnation with 5, 10 and 20% of Ni (m/m). They were characterized by energy dispersive X-ray fluorescence spectrometry (EDX), X-ray diffraction (XRD), temperature-programmed reduction (TPR), thermogravimetric analysis (TGA), adsorption and desorption of N_2 at 77 K, and transmission electron microscopy (TEM). The catalytic activity in relation to the methane conversion reaction was evaluated at 500 °C for 0.5 h. The addition of 10 and 20% of nickel to the clay led to a disordered bentonite structure, characterized by the disappearance of the 001 reflection on the X-ray diffractograms, with a consequent increase in the interaction between nickel oxide and clay (TPR). All catalysts synthesized showed catalytic activity in relation to the conversion of methane to form ordered carbon. The catalyst with 20% of nickel had the highest activity, with 74% of methane conversion.

Keywords: bentonite, delamination, nickel catalysts, methane decomposition

Introduction

Bentonite is an aluminum phyllosilicate comprised essentially of a mixture of smectite clay minerals, such as montmorillonite (the main clay mineral constituent),[1,2] hectorite, saponite, brendelite and nontronite.[3,4] It is applied in several different areas since it is an abundant mineral resource of low cost, and it is environmentally benign, selective and chemically stable. It has specific physical-chemical properties, including swelling capacity and a high surface area for adsorption and ionic exchange.[2,4-8]

The properties of these clay minerals can be altered through modifications in the synthesis process.[9,10] Thus, these materials are widely used in heterogeneous catalysis, acting as catalysts and/or a catalyst support.[11] Studies using clays in several reactions including oligomerization,[5] hydrogenation,[12,13] hydroconversion,[14] autothermal reforming,[15] CO and CO_2 methanation,[16] dry reforming of methane,[17] and so on, have been reported.

Several authors have reported studies on methane reforming employing Ni, Ni-Ce, Ni-Pr, Ni-Zr, Ni-Al, Fe and Cu-based catalysts, anchored on clay, such as smectite, attapulgite and palygorskite.[7,8,18-23] Methane conversions of 0 to 100% have been reported, depending on the type of clay, metal and reaction conditions employed. Chen *et al.*[22] tested the use of palygorskite-based catalysts with 8% of Ni and 0-20% of Al in the dry reforming of methane at 700 °C and observed that the insertion of Al inhibited the sintering of nickel particles, improving the catalytic activity and reaching 100% of methane conversion.

Liu *et al.*[7] reported the dry reforming of methane using Ni/Fe-natural clay and Ni/Cu-natural clay catalysts. The authors observed that pillaring with Fe and Cu influenced the type of support porosity, the distribution and stability of the Ni particles and, as a result, the catalytic activity and selectivity. Mofrad *et al.*,[8] when investigating the catalytic performance of Ni catalysts supported on pillared bentonite in the dry reforming of methane, observed that an increase in the Ni content in the support improved the methane conversion and the catalyst with 15% Ni/pillared bentonite presented 68.75% conversion when tested at 700 °C. Baraka *et al.*[24] showed that natural Ni-rich clay minerals, obtained from natural nickel lateritic ores originating from Niquelândia (Brazil), without a purification step, could be

*e-mail: rayssa.motta@iqb.ufal.br, rayssamotta166@gmail.com
Editor handled this article: Jaísa Fernandes Soares

used to produce syngas when tested in the methane dry reforming reaction at 800 °C.

Studies using natural clay in the catalytic methane decomposition are still sparsely reported in the literature and the catalysts conventionally employed in this reaction include Ni, Co and Fe anchored in silica and alumina.[25,26] However, studies employing metallic catalysts supported on non-oxides, such as commercial carbonaceous materials (carbon nanotubes (CNTs), activated carbon and carbon black) or obtained from renewable natural sources such as lignocellulosic biomass, are reported in the literature.[27-29] Esmizadeh *et al*.[30] reported that catalysts with 25% Fe/montmorillonite were used for the growth of carbon nanotubes through the deposition of chemical methane vapor. This study shows that the type of organo-modification of the clay before the insertion of Fe affected the purity, diameter, length and yield of the carbon nanotubes formed. The catalytic activity of K10 montmorillonite (K10-Mt) as a substrate during the chemical vapor deposition (CVD) using methane to produce nanocarbon was recently investigated by Gubernat and Zambrzycki.[31] The authors found that the CVD process at 850 °C resulted in the deposition of different carbon deposits (bulb-like, finer and slender nanocarbon and CNT) depending on the pre-treatment applied to the K10-Mt. It is worth mentioning that other types of clays, synthetic ones, such as LDHs (double layered hydroxides), or the 'hydrotalcite-like compounds' have been used as precursors of supported metallic catalysts and applied in the decomposition of methane.[32-37]

It should also be noted that the catalytic methane decomposition process produces CO_x-free H_2 and carbon, which can be ordered and nanotubes and nanofibers can be formed, that is, materials with several applications and high aggregated value.[38-41] Thus, in this study, the synthesis and characterization of Ni-based catalysts, with different concentrations, anchored on bentonite clay, were carried out. The catalytic activity was tested in the methane conversion reaction for the production of ordered carbon.

Experimental

Synthesis of catalysts

Nickel catalysts anchored on bentonite clay were prepared following the conventional impregnation method. Bentonite clay (BSI) obtained from the company Proquímios (Bangu, Rio de Janeiro, Brazil) was chosen as the raw material. Its chemical composition, determined by energy dispersive X-ray fluorescence spectrometry (EDX), in mass percentage terms, was 56.56% SiO_2, 27.82% Al_2O_3, 5.16% Fe_2O_3, 1.59% MgO, 4.19% CaO, 2.89% Na_2O, 1.31% TiO_2, 0.47% K_2O, 0.01% ZnO. The cation exchange capacity (CEC) was between 83.3 and 88.9 meq *per* 100 g of clay (determined according to ASTM C 837-09 standard),[42,43] and BET specific surface area (S_{BET}) = 45 $m^2 g^{-1}$. In this procedure, 1 g of BSI, without previous treatment, was added to 50 mL of $Ni(NO_3)_2.6H_2O$ solutions with different concentrations (0.017, 0.034 and 0.068 mol L^{-1}) (Oakwood Chemical, Estill, South Carolina, USA) and the mixture was kept under shaking at 60 °C for 24 h. The sample was then dried in a rotary evaporator (75 °C), calcinated (500 °C/4 h) and sieved using an 80 mesh (180 μm diameter) sieve. The catalysts were named xNiBSI, where x refers to 5, 10 or 20% of Ni (theoretical content in m/m) in relation to the mass of BSI clay used in the impregnation. For comparison purposes, the bentonite clay was suspended in deionized water and the same experimental procedure used for the catalysts was applied, but without the presence of nickel. This sample was named BSI-500.

Characterization

The chemical composition was obtained with an energy dispersive X-ray fluorescence spectrometer (Shimadzu, Kyoto, Japan), model EDX 7000, operating at 50 kV, with a 10 mm collimator, under a vacuum atmosphere.

X-ray diffraction (XRD) patterns were obtained with the aid of a diffractometer (Shimadzu, Kyoto, Japan), model XRD 7000, with Cu Kα radiation, voltage of 30 kV and current of 30 mA. Scans were carried out at intervals of 2θ between 3° and 90°, with a step of 0.02° and velocity of 2° *per* min. The basal spacing values were calculated according to Bragg's law ($d001 = \lambda/2\sin\theta$; d001 is the basal spacing in the diffraction index (001) and $\lambda = 0.15418$ nm), and the crystallite size of NiO was estimated based on the plane (200) of NiO at $2\theta = 43.3°$ using the Scherrer equation.

The temperature programmed reduction (TPR) measurements were performed using a multipurpose analytical system SAMP3 (Termolab, Rio de Janeiro, Brazil), equipped with a thermal conductivity detector (TCD). For these measurements, approximately 0.05 g of the sample were heated from ambient temperature up to 800 °C, at a heating rate of 10 °C min^{-1}, using a gas mixture of 5% of H_2/95% of N_2 flowing at a rate of 30 mL min^{-1}. The TPR curves were deconvoluted with the Gaussian function and the area distributions were calculated based on the integration of the area under the TPR-H_2 curves (available in the computer software program OriginPro 2019).[44]

The thermogravimetric analysis (TGA) was carried out with a TA Instruments analyzer (New Castle, Delaware, USA), model SDT650, under an oxidizing atmosphere

with a flow of 50 mL min^{-1} employing a heating rate of 10 °C min^{-1}, to characterize the catalysts before and after the methane decomposition reaction.

The structural characterization was conducted based on data on the adsorption and desorption of N_2 at 77 K, employing a Quantachrome analyzer (Boynton Beach, Florida, USA). For each analysis, approximately 0.1 g of the sample was degassed at 423.15 K for 3 h in order to remove the moisture content and adsorbed gases from the catalyst surface. The standard Brunauer-Emmett-Teller (BET) method was used to calculate the specific surface area while the pore diameter distribution and volume were calculated based on desorption isotherms employing the Barrett-Joyner-Halenda (BJH) method.

Methane decomposition

The catalytic reactions for methane conversion were carried out under atmospheric pressure at 500 °C, in a fixed-bed tubular quartz reactor inserted in a vertical oven with temperature control (Figure 1). Initially, 0.05 g of the catalyst was reduced under a flow of H_2 at 500 °C for 1 h, with a heating rate of 10 °C min^{-1}. After the reduction, the methane conversion started with the passage of 35 mL min^{-1} of the mixture N_2:CH_4 (6:1 v/v) for 0.5 h, corresponding to 28.021 mg of carbon in contact with the catalyst.

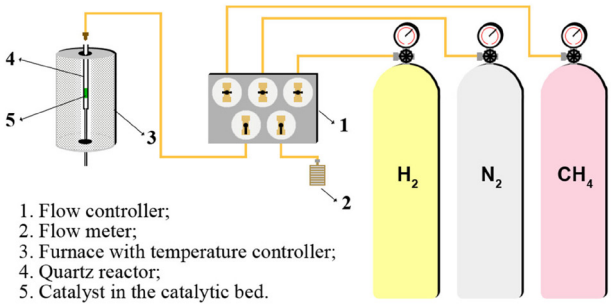

Figure 1. Schematic of the experimental setup.

After the catalytic tests, the catalysts were characterized by transmission electron microscopy (TEM), Raman spectroscopy and TGA in order to obtain information on the carbon formed and methane conversion, respectively. It was considered that all of the methane that passed through the catalyst was decomposed to solid carbon ($C_{(s)}$) and hydrogen gas ($H_{2(g)}$). Thus, the experimental value for $C_{(s)}$ determined by TGA was attributed to catalytic activity (with a total theoretical carbon mass of 28.021 mg in contact with the catalyst in 0.5 h).

Raman spectroscopy was carried out at ambient temperature using a LabRAM HR Evolution spectrometer, equipped with a Synapse detector manufactured by Horiba (Loos, France), using a 785 nm laser as an excitement source and an objective lens (100× magnification). The spectra were obtained with 20 acquisitions in the range of 1000 to 1800 cm^{-1}, using a spectrometric grating of 300 g mm^{-1}.

TEM measurements of the catalysts before and after the methane decomposition were performed on a FEI Tecnai G2 Spirit TWIN transmission electron microscope (Hillsboro, USA), operated at an accelerating voltage of 120 kV, to determine the morphology of the deposited carbon. Prior to the TEM analysis the samples were first dispersed ultrasonically in water at room temperature. A drop of the suspension was then placed on a lacey carbon-coated Cu grid to obtain the images. The carbon deposits were analyzed using ImageJ software.[45]

Results and Discussion

The chemical composition of the samples, determined by EDX, are shown in Table 1. All samples contained the oxides characteristic of bentonite clay: SiO_2, Al_2O_3, Fe_2O_3, MgO, CaO and K_2O.[46] SiO_2 and Al_2O_3 constitute the tetrahedral and octahedral sheets, respectively, of the clay layers. The main octahedral cation of dioctahedral smectites is aluminum, which may contain some cations, such as magnesium and iron.[4,31] Also, based on the data in Table 1, the formation of NiO was observed, and the experimental contents were 8.50, 14.62 and 25.62% for the catalysts 5NiBSI, 10NiBSI and 20NiBSI, respectively. These values are higher than the theoretical contents calculated due to

Table 1. Chemical composition of samples

Sample	Chemical composition / (% m/m)									
	SiO_2	Al_2O_3	Fe_2O_3	MgO	CaO	Na_2O	K_2O	TiO_2	ZnO	NiO
BSI	56.56	27.82	5.16	1.59	4.19	2.89	0.47	1.31	0.02	0.01
BSI500	56.36	28.21	4.96	1.62	4.16	2.94	0.48	1.25	0.02	0.01
5NiBSI	51.75	25.65	4.86	1.39	4.01	2.17	0.45	1.21	0.01	8.50
10NiBSI	48.45	23.94	4.22	1.39	3.72	2.20	0.40	1.06	0.01	14.62
20NiBSI	42.70	20.71	3.57	1.13	3.29	1.70	0.36	0.93	–	25.62

BSI: bentonite clay.

the use of bentonite clay without heat treatment to remove the adsorbed water.

In the diffractogram of the BSI sample (Figure 2), reflections characteristic of clay minerals of the type smectite (JCPDS, No. 00-060-0318) and kaolinite (JCPDS, No. 14-0164) were observed, with the presence of quartz minerals (JCPDS 46-1045) and calcite (JCPDS, No. 05-0586). For the xNiBSI catalysts, besides the BSI reflections, diffraction peaks were observed at 2θ = 37.08°, 43.03°, 62.9° and 79.38°, attributed to the planes of the cubic phase of NiO (JCPDS No. 01-071-1179).

In the case of the BSI-500 sample there was the disappearance of the reflection 001, located at 2θ lower than 10°, referring to the clay mineral smectite. This is associated with the total delamination of the clay layers, with the loss of crystallinity and laminar distribution,[5,6,18,30] as also suggested by the rearrangement of the clay layers through edge-face or edge-edge interactions.[10,14,18,19] This can be attributed to the sample calcination at 500 ºC, where dehydration and dehydroxylation of the clay layers occurred[18,47] with the consequent collapse of the space between the layers.[18,48,49]

The 5NiBSI sample showed a decrease in the diffraction intensity of the reflection 001 at 2θ = 5.5°, suggesting that a smaller amount of nickel oxide minimized the delamination process, partially maintaining the organizational structure of the bentonite, since samples with a greater amount of nickel oxide (10NiBSI and 20NiBSI) showed a loss of crystal structure. The NiO crystallite diameter increased with an increase in the amount of nickel oxide in the samples. The 5NiBSI, 10NiBSI and 20NiBSI samples presented crystallite sizes of around 9.03, 13.6 and 31.0 nm, respectively, calculated by the Scherrer equation.[16]

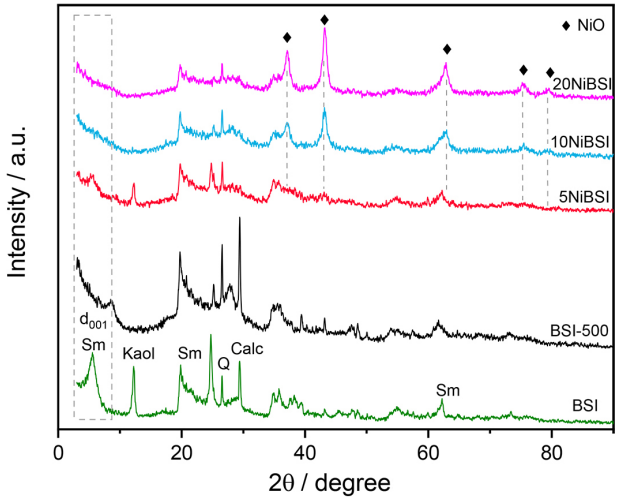

Figure 2. XRD diffractograms for samples BSI, BSI-500, 5NiBSI, 10NiBSI and 20NiBSI (Sm: smectite, Kaol: kaolinite, Q: quartz, Calc: calcite).

The microstructural morphology of the samples was evaluated by TEM (Figure 3). The BSI clay showed aggregated and compact particles, with a structure in the form of plates, of irregular morphology, although there are plates with regular profiles, with a well-defined contour, of hexagonal shape. The BSI-500 presented less dense plates of varying sizes, with some spaces between them, suggesting that the clay layers adopted the face-edge and edge-edge structural organizations, indicating that the delamination process had occurred, as observed from the XRD results. The 10NiBSI (not shown here) and 20NiBSI catalysts presented structures similar to that of BSI-500, with more open structures, the presence of spaces with different sizes (yellow lines) and the presence of nickel oxide nanoparticles in their structures (red arrows in Figure 3).

The TPR results showed hydrogen consumption starting in the region of 270 °C and extending to temperatures

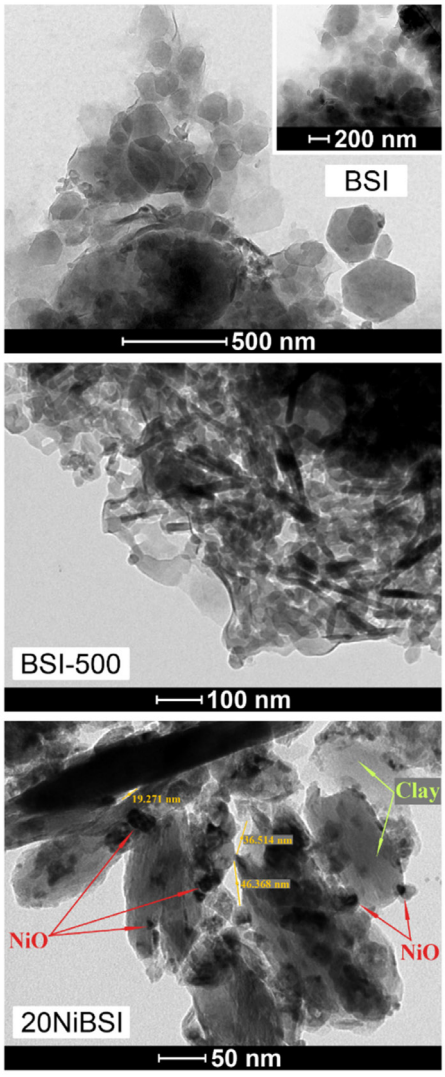

Figure 3. TEM images of the samples: BSI, BSI-500 and 20NiBSI.

above 800 °C (Figure 4a). The BSI sample presented H_2 consumption between 430 and 800 °C, which is associated with the reduction of the metal oxides in the bentonite structure, possibly iron oxides and other cations, and can also be attributed to the dehydroxylation of the –OH groups of the lamellae.[18]

For the xNiBSI catalysts, the reduction temperature region started at 270 °C and extended to temperatures above 800 °C, with different curve profiles and hydrogen consumption peaks. These differences may be related to the crystalline size of NiO and/or the reduction of species of nickel oxides with different forces of interaction with the bentonite.[50] From the deconvolution of the TPR curves of the catalysts (Figure 4b) three peaks for the Gaussian fit were determined, namely α, β and γ, and attributed to the reduction of the nickel oxides interacting with bentonite in weak (270 to 420 °C), medium (420 to 580 °C) and strong (580 to 800 °C) interactions.

Areas referring to each type of interaction between the metal and the bentonite were calculated and the relation of these areas to the total area under the curve was determined, the total area being attributed to 100% of the reduced nickel oxide (Table 2). The 5NiBSI catalyst showed a well-defined α reduction peak in the interval between 270 and 405 °C, corresponding to 100% of nickel oxide with a weak interaction with the bentonite. Low hydrogen consumption in the areas of the β and γ reduction peaks observed for 5NiBSI were associated with bentonite, since the nickel concentration in this catalyst was low.

An increase in the nickel oxide content of the catalysts promoted a higher consumption of hydrogen with a shift to temperatures higher than 400 °C, promoting a stronger interaction of nickel oxide with bentonite. In the case of the 10NiBSI catalyst, a gradual increase was observed in the percentage of nickel oxide reduction, with values of 5% for weak interaction, 45% for medium interaction and 50% for strong interaction with bentonite.

However, the same behavior was not observed for the 20NiBSI catalyst, which presented values of 10, 60 and 30% for weak, medium and strong interactions, respectively. These differences in the metal-support interaction forces were attributed to the size and location of the crystallites of nickel oxide and bentonite. In the 5NiBSI catalyst, partially delaminated, the nickel oxide is located at the external surface of the clay, with weak interaction, and thus it is easily reduced. In the case of the 10NiBSI and 20NiBSI catalysts, the delamination promoted a rearrangement of the lamellae and the nickel oxide is located at the external edges of the lamellae, in the face-edge and edge-edge aggregates of the clay, as shown in Figure 5. Thus, there are more lamellae available for

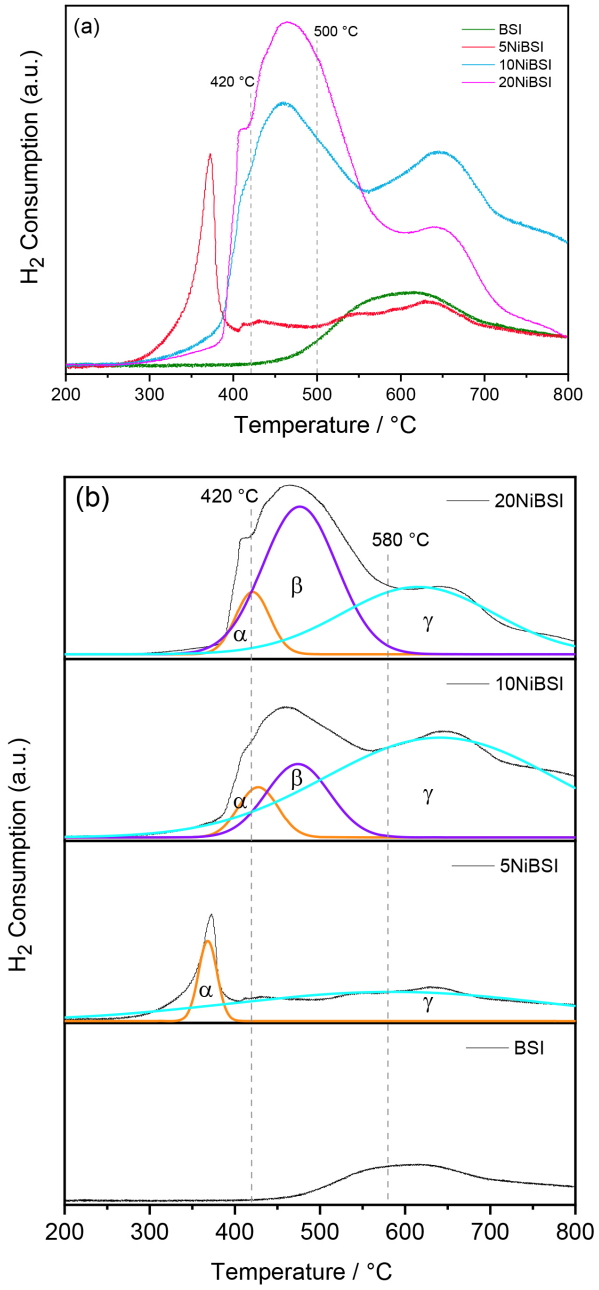

Figure 4. (a) TPR and (b) deconvolution of TPR curves for samples BSI, BSI-500, 5NiBSI, 10NiBSI, and 20NiBSI.

interaction with the nickel oxide, increasing the metal-clay interaction and, consequently, the reduction temperature. In the case of the 20NiBSI catalyst, due to the higher nickel concentration, the delamination of the clay layers facilitated the aggregation of the metal particles, that is, the growth of the nickel particle size, which minimized, through the stereo effect, the interaction between the clay lamellae and the nickel oxide.

Based on the XRD and TPR data, the increased force of the interaction between nickel oxide and bentonite, observed for 10NiBSI and 20NiBSI catalysts, was

attributed to the total delamination of the bentonite, which promoted higher accessibility and a greater number of sites for interaction.

Table 2. Percentages of nickel oxide showing weak, medium and strong interactions with bentonite in the 5NiBSI, 10NiBSI and 20NiBSI catalysts

Catalyst	Reduced nickel oxide / %		
	Weak interaction (< 420 °C)	Medium interaction (420-580 °C)	Strong interaction (> 580 °C)
5NiBSI	100	–	–
10NiBSI	5	45	50
20NiBSI	10	60	30

BSI: bentonite clay.

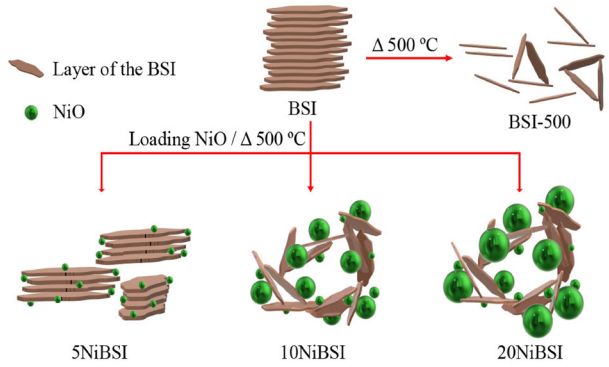

Figure 5. Representation of clay (BSI) after thermal treatment and anchoring of nickel oxide.

Figure 6 shows the TGA results obtained for the samples. The BSI sample presented 17.48% of total mass loss, typical of smectite, with 7.7% of mass loss below 100 °C, related to water, and 9.71% of mass loss between 100 and 680 °C, related to the water of hydration of the interlayer cations and structural water of the hydroxyl groups (dehydroxylation).[48,49]

With the anchoring of nickel oxide to bentonite a lower mass loss related to structural water was observed, indicating that the nickel oxide is bound to these structural hydroxyls, stabilizing the thermal decomposition of these groups. This could be observed when the nickel content was increased from 5 to 10% and 20%, with decreases in the mass loss occurs, from 11.10 to 3.40% and 2.67%, respectively, related to structural water (Table 3). This observation is consistent with the delamination of the 10NiBSI and 20NiBSI catalysts, exposing these hydroxyls, facilitating the formation of new more stable bonds with the nickel oxide particles and favoring the medium and strong metal-support interactions, as seen in the TPR results.

The isotherms for the N_2 adsorption and desorption at 77 K revealed changes in the textural properties of the materials (Figures 7 and S1, Supplementary Information

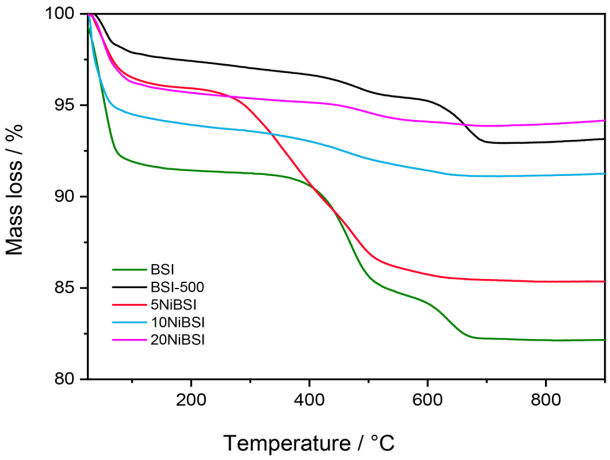

Figure 6. TGA results for BSI, BSI-500, 5NiBSI, 10NiBSI, and 20NiBSI samples.

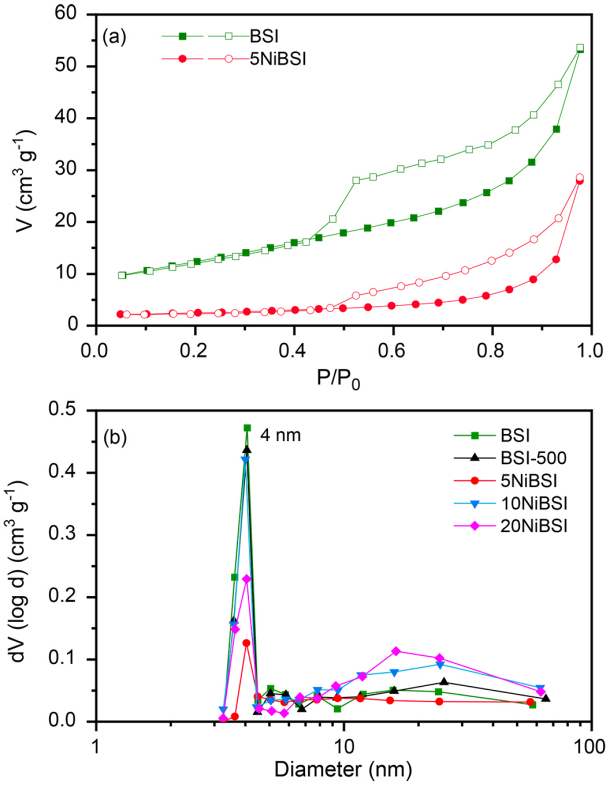

Figure 7. (a) Isotherms of N_2 adsorption and desorption at 77 K and (b) pore diameter distribution of samples BSI, BSI-500, 5NiBSI, 10NiBSI, and 20NiBSI.

section). The profiles of the adsorption isotherms were similar for all samples and corresponded to type VI, according to the International Union of Pure and Applied Chemistry (IUPAC) classification, presenting H4 hysteresis loops[51] typical of material comprised of plates containing pores in the form of slits. The shape of the hysteresis loops and the isotherm profiles indicate that the materials have a mesoporous structure, suggesting the presence of macropores and micropores[52] and that

the solid particles are comprised of laminar aggregates, confirming the delamination process. The hysteresis loop was preserved in all samples, although a decrease in the adsorption capacity of the 5NiBSI catalyst in comparison to BSI was observed. For all samples, a pore distribution of between 2 and 50 nm was observed (Figure 7b), with a concentration of pores of around 4.0 nm, confirming the mesoporosity of these materials. Only the 10NiBSI and 20NiBSI catalysts, which underwent total delamination, showed a distribution of pores with diameters in the range to 10 to 60 nm. This is because the rearrangement of the bentonite layers into edge-face or edge-edge aggregates[10,14,19] allowed the formation of new spaces (interparticle spaces with porosity in the range of 2-50 nm) and the arrangement/assembly of these aggregates may lead to inter-aggregated pores in the size range of mesopores and macropores (> 50 nm).[52-54] Thus, this reorganization of lamellae favored the dispersion and distribution of nickel oxide on the bentonite surface.[19]

Table 3 shows the data obtained for the surface area of the samples. It was observed that the calcination of bentonite without nickel oxide (BSI-500) promoted a slight decrease in the surface area due to the removal of different types of water content and consequent delamination, as seen in the TGA and XRD results, respectively.

In the case of the 5NiBSI catalyst there was a decrease in the surface area and the pore volume, attributed to the location of the nickel oxide particles in the bentonite. Therefore, the nickel oxide particles, besides being on the external surface of the bentonite, are also on the edges of the lamellae, decreasing and/or blocking the bentonite pores.[7,8,17] The 10NiBSI and 20NiBSI catalysts presented specific surface areas and pore volumes similar to those of BSI-500, due to the reorganization of the lamellae after delamination.[10,18,19]

The small difference between the surface areas observed for the 10NiBSI and 20NiBSI catalysts was attributed to the crystallite size of the nickel oxide (Table 3), since larger particles lead to a lower dispersion and a decrease in the surface area.[8,16,55]

The TGA results for the catalysts after the methane conversion tests provided quantitative and qualitative data regarding the carbon structures formed, which were employed to calculate the methane conversion at 500 ºC for 0.5 h (Figure 8 and Table 3). All catalysts presented mass loss at around 650 °C, characteristic of the thermal decomposition of ordered carbon in the form of nanotubes.[56-58]

These ordered structures were confirmed through the Raman spectroscopy and TEM. The Raman spectra obtained for the catalysts after the catalytic tests, seen in Figure 8b, showed the D and G bands at 1310 and 1590 cm^{-1}, respectively, characteristic of carbon nanotubes with defective walls.[26,30,59] The values for the ratio between

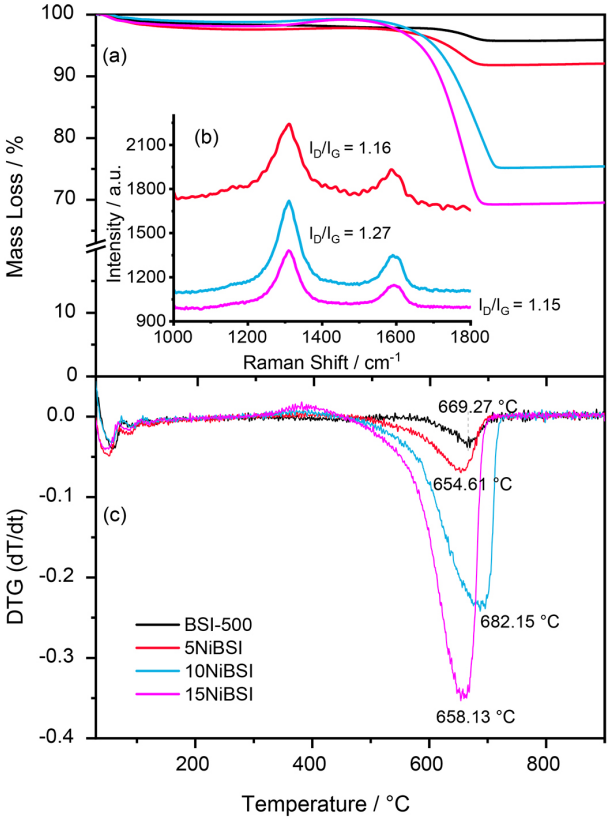

Figure 8. (a) TGA results, (b) Raman spectra and (c) DTG results for BSI-500, 5NiBSI, 10NiBSI, and 20NiBSI after the methane conversion at 500 °C for 0.5 h.

Table 3. Textural properties of the BSI, BSI-500, 5NiBSI, 10NiBSI and 20NiBSI samples and data from TGA for BSI-500, 5NiBSI, 10NiBSI and 20NiBSI before and after the methane decomposition

Sample	S_{BET}[a] / (m^2 g^{-1})	V_p[b] / (cm^3 g^{-1})	Free H_2O mass loss[c] / %	Structural H_2O mass loss[c] / %	C mass loss[d] / %
BSI	45	0.084	7.77	9.71	–
BSI-500	30	0.089	2.15	4.94	2.10
5NiBSI	8	0.050	3.60	11.10	5.94
10NiBSI	48	0.108	5.50	3.40	23.86
20NiBSI	35	0.101	3.67	2.67	29.62

[a]S_{BET}: BET specific surface area; [b]V_p: pore volume; based on TGA data obtained [c]before and [d]after the methane decomposition; BSI: bentonite clay.

the relative intensities of band D and band G (ratio I_D/I_G) were close, indicating similar degrees of crystallinity and graphitization for the nanotubes formed.

Figure 9 shows the brightfield TEM images of the 5NiBSI, 10NiBSI, and 20NiBSI catalysts after methane decomposition at 500 °C for 0.5 h. The carbon structures deposited on the catalysts showed a predominantly tubular form, corroborating the mass loss of carbonaceous material at around 650 °C observed in the TGA.

Dense string-like carbon nanostructures grew on the surface of the 5NiBSI cluster. The higher-magnification image shows hollow-core tubular rope-like carbon structures, confirming the formation of CNTs with open ends. The carbon formations present in 5NiBSI are strongly curved and most are tubular structures in the form of rope. The ends of the carbon structures are open and no Ni particles are observed at the tip or inside the nanotubes, indicating that the formation of carbon on the catalyst surface followed a growth mechanism starting at the base.[60]

In the 5NiBSI catalyst, the Ni particles are not clearly visualized due to the shape of the tube, while in the 10NiBSI, and 20NiBSI catalysts, respectively, the nickel particles have a diamond or pear shape and the Ni particle tail is inserted in the carbon nanotubes/nanofiber.

In the 10NiBSI and 20NiBSI catalysts, after the 30 min of reaction, some of the exposed surfaces of the Ni particles remained clean, indicating that they could continuously decompose the methane to produce carbon and hydrogen nanofibers/nanotubes. In both catalysts multi-walled carbon structures were observed. In the 10NiBSI catalyst, the Ni particles had an average size of 36.88 ± 13.08 nm. The images showed that the outer diameter of the carbon nanotubes is related to the size of the Ni particles, with larger Ni particles promoting larger-diameter carbon nanotubes. The average size of the Ni particle observed in the 20NiBSI catalyst was 37.27 ± 9.38 nm, a value close to the crystallite size calculated by the Scherrer equation, and the average external diameter of the nanotubes was 34.42 ± 9.45 nm.

Different types of nanofibers/nanotubes were formed in 10NiBSI and 20NiBSI. Some had closed ends with Ni particles at their tip, others were open-ended with no Ni particles being observed, while small Ni particles were incorporated in some of the nanotubes. However, for most of the carbon nanofibers/nanotubes the end was filled with Ni particles and the walls of the nanotubes had a fishbone arrangement (Figure 9). Similar results have been reported for Ni/Ce-MCM-41 and Ni-Co-Al catalyst systems by Guevara *et al.*[60] and Fakeeha *et al.*,[40] respectively.

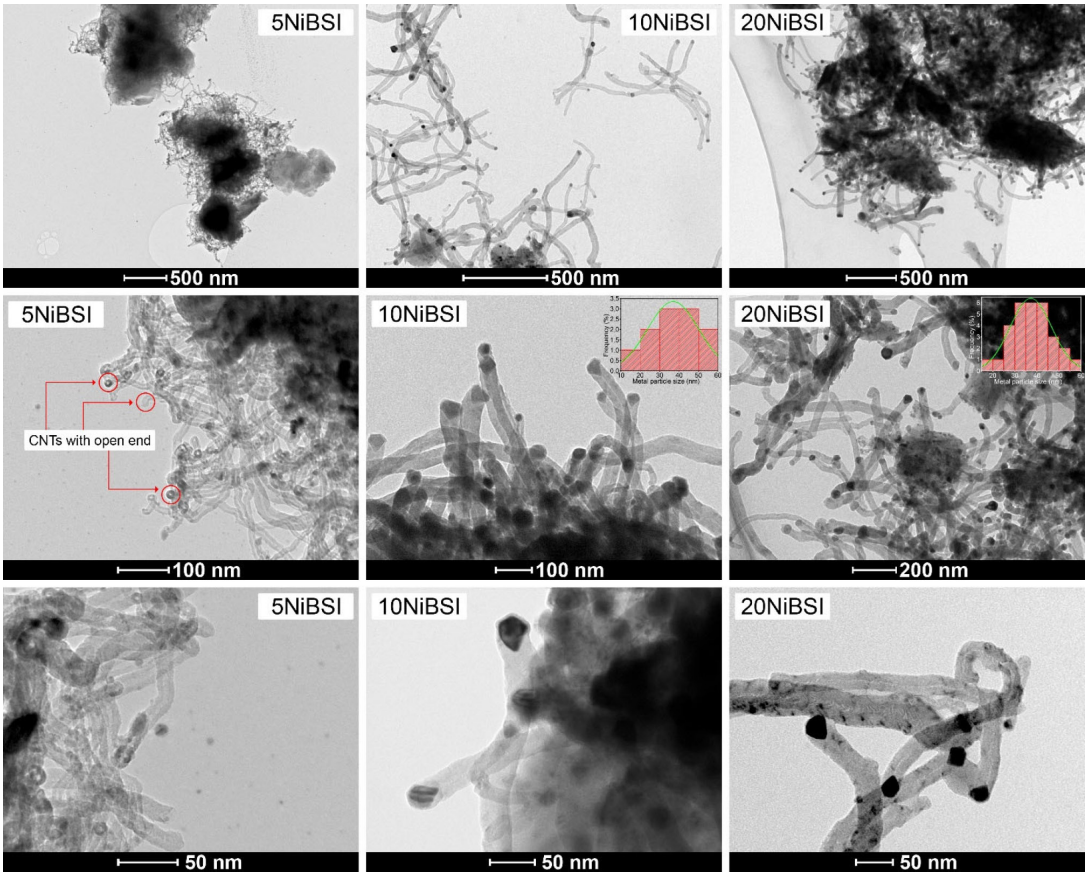

Figure 9. TEM images of carbon nanostructures formed during methane decomposition over the catalysts: 5NiBSI, 10NiBSI, and 20NiBSI.

It was observed that the calcinated clay (BSI-500) presented 4% of methane conversion, attributed to the presence of metal oxides in the clay structure.[18,49] The 5NiBSI, 10NiBSI and 20NiBSI catalysts presented 11, 55 and 74% of methane conversion, respectively (Table 4 and Figure 10). It was observed that an increase in the nickel oxide content of the catalyst provided greater methane conversion and that the textural properties of the catalysts did not influence significantly the catalytic activity.

On comparing our results with those reported by Esmizadeh *et al.*,[30] who employed catalysts based on montmorillonite in methane conversion with and without the presence of hydrogen for the production of carbon nanotubes, it is noteworthy that in the approach reported herein the catalysts are synthesized in a single stage, with no modification of the clay before the Ni insertion.

In comparison with studies reported in the literature on methane reforming over catalysts containing clay and methane decomposition over Ni catalysts anchored on conventional catalytic supports (Table 4), the xNiBSI catalysts synthesized in this study showed similar and/or higher conversions depending on the reaction conditions.

As shown in Table 4, the catalyst 10CeDC (10% Ni and 10% Ce supported on delaminated smectite clay), tested in the dry reforming of methane, presented 60% of methane conversion. This is similar to the value observed for the 10NiBSI catalyst, in which the metal has the same nominal load but was used for the methane conversion reaction. The conventional catalyst evaluated in the methane decomposition reaction, 20Ni-30Fe/Al (20% of Ni and 30% of Fe), reportedly showed 72% of methane conversion.

Thus, the bentonite clay showed potential for use as a catalytic support for methane conversion since the loss

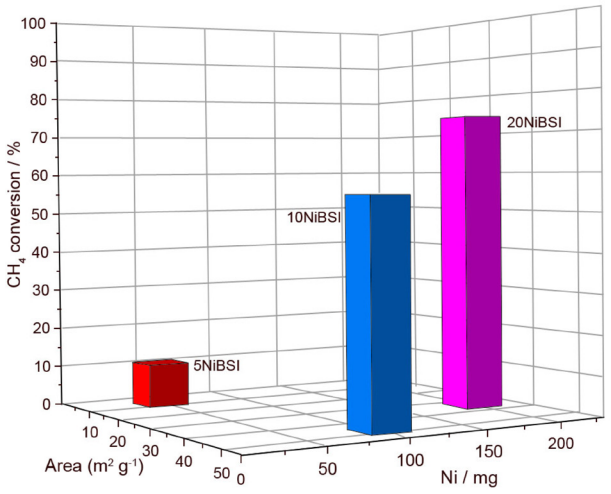

Figure 10. Methane conversion over the 5NiBSI, 10NiBSI and 20NiBSI catalysts.

Table 4. Comparison of the levels of catalytic activity of catalysts containing clay tested in methane dry reforming and conventional catalysts tested in the methane conversion reaction

Clay-based catalysts-dry reforming of methane					
Catalyst	Catalyst mass / mg	Reaction temperature / °C	Feed gas ratio	GHSV / (L g^{-1} h^{-1})	CH_4 conversion / %
Ni-Pr3/Clay[19]	50	700	CH_4/CO_2 (1/1)	96	45
0CeDC[10]	50	700	CH_4/CO_2 (1/1)	96	45
10CeDC[10]	50	700	CH_4/CO_2 (1/1)	96	60
Ni-clay[7]	60	600	CH_4/CO_2/Ar (1/1/8)	100	< 5
Ni/Fe-clay[7]	60	600	CH_4/CO_2/Ar (1/1/8)	100	< 5
Ni-Al/Fe-clay[20]	60	600	CH_4/CO_2/Ar (1/1/8)	100	12.5
	60	700	CH_4/CO_2/Ar (1/1/8)	100	37.5
15% Ni/pillared bentonite[8]	100	700	CH_4/CO_2 (1/1)	12	68.75
Ni8/Al8/Pal[22]	500	500	CH_4/CO_2/Ar (1/1/8)	12	52
	500	700	CH_4/CO_2/Ar (1/1/8)	12	100
Conventional catalysts-methane decomposition					
Ni/SiO_2[38]	40	500	CH_4	90	8
FeMo (5.1)/Al_2O_3[61]	10	750	CH_4	1.5	75
20NCA (Ni-Co-Al_2O_3)[40]	300	700	CH_4	5	69
20Ni-30Fe/Al[62]	300	700	CH_4	5	72
5Ni-BSI (this study)	50	500	CH_4/N_2 (1/6)	42	11
10Ni-BSI (this study)	50	500	CH_4/N_2 (1/6)	42	55
20NiBSI (this study)	50	500	CH_4/N_2 (1/6)	42	74

GHSV: gas hourly space velocity; BSI: bentonite clay.

of its organizational structure (delamination process) had no influence on the catalytic activity and all of the catalysts studied were found to be active in the methane decomposition reaction.

Conclusions

The anchoring of nickel oxide on clay without previous treatment promoted a change in the bentonite structure, the delamination of clay layers, and greater interaction between the nickel oxide and the bentonite. However, the structural alterations did not influence the catalytic activity and all of the catalysts promoted the conversion of methane into products. Thus, the methane conversion over the catalysts based on BSI was directly influenced by the content of nickel oxide reduced at 500 °C. The catalyst with the intermediate concentration of nickel oxide (10NiBSI) was the most promising in relation to the decomposition of methane, when the proportions of nickel oxide and methane conversion are considered.

Supplementary Information

Supplementary data are available free of charge at http://jbcs.sbq.org.br as PDF file.

Acknowledgments

This study was supported by the Conselho Nacional de Desenvolvimento Científico e Tecnológico (CNPq), Coordenação de Aperfeiçoamento de Pessoal de Nível Superior (CAPES) and Fundação de Amparo à Pesquisa do Estado de Alagoas (FAPEAL). RJBM is grateful for the scholarship provided by CNPq. RMA and CBD would like to thank CNPq for the scholarship provided. The authors are grateful to the team at GCAR-IQB, TECNANO, Dyego Maia de Oliveira (MESOMAG-UFPE), Tasso de Oliveira Salles (GNFI-UFAL) and the professors Antônio Osimar S. da Silva (LSCAT-UFAL), Irinaldo Diniz (LABTCOM-UFAL) and Rodrigo José de Oliveira (PCMLab-UEPB) for their contributions.

References

1. Bergaya, F.; Theng, B. K. G.; Lagaly, G.; *Handbook of Clay Science*, 1st ed.; Elsevier Science: Amsterdam, The Netherlands, 2006.
2. Mukherjee, S.; Ghosh, B.; *The Science of Clays: Applications in Industry, Engineering and Environment*; Springer: Dordrecht, The Netherlands, 2013.
3. Shaikh, S. M. R.; Nasser, M. S.; Hussein, I.; Benamor, A.; Onaizi, S. A.; Qiblawey, H.; *Sep. Purif. Technol.* **2017**, *187*, 137. [Crossref]
4. Awad, A. M.; Shaikh, S. M. R.; Jalab, R.; Gulied, M. H.; Nasser, M. S.; Benamor, A.; Adham, S.; *Sep. Purif. Technol.* **2019**, *228*, 115719. [Crossref]
5. Aid, A.; Andrei, R. D.; Amokrane, S.; Cammarano, C.; Nibou, D.; Hulea, V.; *Appl. Clay Sci.* **2017**, *146*, 432. [Crossref]
6. Zhang, W.; Li, M. K. S.; Wang, R.; Yue, P.-L.; Gao, P.; *Langmuir* **2009**, *25*, 8226. [Crossref]
7. Liu, H.; Yao, L.; Hadj Taief, H. B.; Benzina, M.; Da Costa, P.; Gálvez, M. E.; *Catal. Today* **2018**, *306*, 51. [Crossref]
8. Daroughegi Mofrad, B.; Rezaei, M.; Hayati-Ashtiani, M.; *Int. J. Hydrogen Energy* **2019**, *44*, 27429. [Crossref]
9. Bergaya, F.; Lagaly, G.; *Appl. Clay Sci.* **2001**, *19*, 1. [Crossref]
10. Daza, C. E.; Gamba, O. A.; Hernández, Y.; Centeno, M. A.; Mondragón, F.; Moreno, S.; Molina, R.; *Catal. Lett.* **2011**, *141*, 1037. [Crossref]
11. Schoonheydt, R. A.; *Appl. Clay Sci.* **2016**, *131*, 107. [Crossref]
12. Jiang, Y.; Li, X.; Qin, Z.; Ji, H.; *Chin. J. Chem. Eng.* **2016**, *24*, 1195. [Crossref]
13. Ren, S.-B.; Zhang, S.; Zhao, R.; Wang, Z.-C.; Lei, Z.-P.; Pan, C.-X.; Kang, S.-G.; Shui, H.-F.; *J. Fuel Chem. Technol.* **2018**, *46*, 171. [Crossref]
14. Amaya, J.; Suarez, N.; Moreno, A.; Moreno, S.; Molina, R.; *New J. Chem.* **2020**, *44*, 2966. [Crossref]
15. Akri, M.; Achak, O.; Granger, P.; Wang, S.; Batiot-Dupeyrat, C.; Chafik, T.; *J. Cleaner Prod.* **2018**, *171*, 377. [Crossref]
16. Lu, X.; Gu, F.; Liu, Q.; Gao, J.; Liu, Y.; Li, H.; Jia, L.; Xu, G.; Zhong, Z.; Su, F.; *Fuel Process. Technol.* **2015**, *135*, 34. [Crossref]
17. Liu, H.; Da Costa, P.; Hadj Taief, H. B.; Benzina, M.; Gálvez, M. E.; *RSC Adv.* **2018**, *8*, 19627. [Crossref]
18. Daza, C. E.; Kiennemann, A.; Moreno, S.; Molina, R.; *Appl. Catal., A* **2009**, *364*, 65. [Crossref]
19. Gamba, O.; Moreno, S.; Molina, R.; *Int. J. Hydrogen Energy* **2011**, *36*, 1540. [Crossref]
20. Liu, H.; Hadjltaief, H. B.; Benzina, M.; Gálvez, M. E.; Da Costa, P.; *Int. J. Hydrogen Energy* **2019**, *44*, 246. [Crossref]
21. Liu, H.; Da Costa, P.; Hadj Taief, H. B.; Benzina, M.; Gálvez, M. E.; *Int. J. Hydrogen Energy* **2017**, *42*, 23508. [Crossref]
22. Chen, Y.; Chen, T.; Liu, H.; Zhang, P.; Wang, C.; Dong, S.; Chen, D.; Xie, J.; Zou, X.; Suib, S. L.; Li, C.; *Appl. Clay Sci.* **2020**, *188*, 105498. [Crossref]
23. Wei, Y.; Song, M.; Yu, L.; Meng, F.; Xiao, J.; *Int. J. Hydrogen Energy* **2019**, *44*, 20056. [Crossref]
24. Baraka, S.; Bouearan, K.; Caner, L.; Fontaine, C.; Epron, F.; Brahmi, R.; Bion, N.; *J. CO2 Util.* **2021**, *52*, 101696. [Crossref]
25. Reddy, P. V. L.; Kim, K.-H.; Song, H.; *Renewable Sustainable Energy Rev.* **2013**, *24*, 578. [Crossref]
26. Pudukudy, M.; Yaakob, Z.; *Chem. Eng. J.* **2015**, *262*, 1009. [Crossref]

27. Dipu, A. L.; *Int. J. Energy Res.* **2021**, *45*, 9858. [Crossref]
28. Henao, W.; Cazaña, F.; Tarifa, P.; Romeo, E.; Latorre, N.; Sebastian, V.; Delgado, J. J.; Monzón, A.; *Chem. Eng. J.* **2021**, *404*, 126103. [Crossref]
29. Yan, Q.; Ketelboeter, T.; Cai, Z.; *Molecules* **2022**, *27*, 503. [Crossref]
30. Esmizadeh, E.; Yousefi, A. A.; Naderi, G.; Milone, C.; *Appl. Clay Sci.* **2015**, *118*, 248. [Crossref]
31. Gubernat, M.; Zambrzycki, M.; *Appl. Clay Sci.* **2021**, *211*, 106178. [Crossref]
32. Shi, Z.; Wan, C.; Huang, M.; Pan, J.; Luo, R.; Li, D.; Jiang, L.; *Int. J. Hydrogen Energy* **2020**, *45*, 17299. [Crossref]
33. Ashok, J.; Subrahmanyam, M.; Venugopal, A.; *Int. J. Hydrogen Energy* **2008**, *33*, 2704. [Crossref]
34. Wan, C.; Shi, Z.; Huang, M.; Pan, J.; Luo, R.; Li, D.; Jiang, L.; *Int. J. Hydrogen Energy* **2021**, *46*, 3833. [Crossref]
35. Sikander, U.; Samsudin, M. F.; Sufian, S.; KuShaari, K. Z.; Kait, C. F.; Naqvi, S. R.; Chen, W. H.; *Int. J. Hydrogen Energy* **2019**, *44*, 14424. [Crossref]
36. García-Sancho, C.; Guil-López, R.; Sebastián-López, A.; Navarro, R. M.; Fierro, J. L. G.; *Int. J. Hydrogen Energy* **2018**, *43*, 9607. [Crossref]
37. Guo, Z.; Zheng, J. E.; Liu, Y.; Chu, W.; *Appl. Catal., A* **2018**, *555*, 1. [Crossref]
38. Takenaka, S.; Kobayashi, S.; Ogihara, H.; Otsuka, K.; *J. Catal.* **2003**, *217*, 79. [Crossref]
39. Takenaka, S.; Ishida, M.; Serizawa, M.; Tanabe, E.; Otsuka, K.; *J. Phys. Chem. B* **2004**, *108*, 11464. [Crossref]
40. Fakeeha, A. H.; Khan, W. U.; Al-Fatesh, A. S.; Abasaeed, A. E.; Naeem, M. A.; *Int. J. Hydrogen Energy* **2015**, *40*, 1774. [Crossref]
41. Fan, Z.; Weng, W.; Zhou, J.; Gu, D.; Xiao, W.; *J. Energy Chem.* **2021**, *58*, 415. [Crossref]
42. ASTM C 837-09: *Standard Test Method for Methylene Blue Index of Clay*, 2009.
43. Almeida, A. Z. F.: *Caracterização de Bentonita Sódica e seu Comportamennto Coloidal na Presença de Polifosfato*; MSc. Dissertation, Universidade Estadual da Paraíba, Campina Grande, Paraíba, Brazil, 2018. [Crossref]
44. *Origin*, version 2019b; OriginLab, Northampton, USA, 2019.
45. Rasband, W. S.; *ImageJ*, version 1.53e; U. S. National Institutes of Health, Bethesda, Maryland, USA, 2020.
46. Muñoz, H. J.; Blanco, C.; Gil, A.; Vicente, M.-A.; Galeano, L. A.; *Materials* **2017**, *10*, 1364. [Crossref]
47. Gopal Mishra, B.; Ranga Rao, G.; *Microporous Mesoporous Mater.* **2004**, *70*, 43. [Crossref]
48. Heller-Kallai, L. In *Developments in Clay Science*, vol. 5; Bergaya, F.; Lagaly, G., eds.; Elsevier Ltd.: Amsterdam, The Netherlands, 2013, ch. 10.2. [Crossref]
49. Alabarse, F. G.; Conceição, R. V.; Balzaretti, N. M.; Schenato, F.; Xavier, A. M.; *Appl. Clay Sci.* **2011**, *51*, 202. [Crossref]
50. Gac, W.; Zawadzki, W.; Słowik, G.; Sienkiewicz, A.; Kierys, A.; *Microporous Mesoporous Mater.* **2018**, *272*, 79. [Crossref]
51. Sing, K. S. W.; Everet, D. H.; Haul, R. A. W.; Moscou, L.; Pierotti, R. A.; Rouquérol, J.; Siemieniewska, T.; *Pure Appl. Chem.* **1985**, *57*, 603. [Crossref]
52. Shah, L. A.; Valenzuela, M. G. S.; Farooq, M.; Khattak, S. A.; Díaz, F. R. V.; *Appl. Clay Sci.* **2018**, *162*, 155. [Crossref]
53. Salles, F.; Douillard, J. M.; Denoyel, R.; Bildstein, O.; Jullien, M.; Beurroies, I.; Van Damme, H.; *J. Colloid Interface Sci.* **2009**, *333*, 510. [Crossref]
54. Shah, L. A.; Farooq, M.; Carvalho, F. M. S.; da Silva Valenzuela, M. G.; Valenzuela Díaz, F. R.; *Arabian J. Sci. Eng.* **2018**, *43*, 373. [Crossref]
55. Jiang, Y.; Huang, T.; Dong, L.; Qin, Z.; Ji, H.; *Chin. J. Chem. Eng.* **2018**, *26*, 2361. [Crossref]
56. Wang, H.; Ren, F.; Liu, C.; Si, R.; Yu, D.; Pfefferle, L. D.; Haller, G. L.; Chen, Y.; *J. Catal.* **2013**, *300*, 91. [Crossref]
57. Awadallah, A. E.; Aboul-Enein, A. A.; Aboul-Gheit, A. K.; *Energy Convers. Manage.* **2014**, *77*, 143. [Crossref]
58. Awadallah, A. E.; Aboul-Enein, A. A.; Kandil, U. F.; Taha, M. R.; *Mater. Chem. Phys.* **2017**, *191*, 75. [Crossref]
59. Takenaka, S.; Ogihara, H.; Yamanaka, I.; Otsuka, K.; *Appl. Catal., A* **2001**, *217*, 101. [Crossref]
60. Guevara, J. C.; Wang, J. A.; Chen, L. F.; Valenzuela, M. A.; Salas, P.; García-Ruiz, A.; Toledo, J. A.; Cortes-Jácome, M. A.; Angeles-Chavez, C.; Novaro, O.; *Int. J. Hydrogen Energy* **2010**, *35*, 3509. [Crossref]
61. Torres, D.; Pinilla, J. L.; Lázaro, M. J.; Moliner, R.; Suelves, I.; *Int. J. Hydrogen Energy* **2014**, *39*, 3698. [Crossref]
62. Al-Fatesh, A. S.; Fakeeha, A. H.; Khan, W. U.; Ibrahim, A. A.; He, S.; Seshan, K.; *Int. J. Hydrogen Energy* **2016**, *41*, 22932. [Crossref]

Submitted: March 4, 2022
Published online: November 18, 2022